ChemPubSoc Europe

DOI: 10.1002/cssc.201700317

CHEMSUSCHEM Full Papers

Facile Synthesis of Rod-like $Cu_{2-x}Se$ and Insight into its Improved Lithium-Storage Property

He Li, Jiali Jiang, Feng Wang, Jianxing Huang, Yunhui Wang, Yiyong Zhang, and Jinbao Zhao*[a]

A rod-like $Cu_{2-x}Se$ is synthesized by a facile water evaporation process. The electrochemical reaction mechanism is investigated by ex situ X-ray diffraction (XRD). By adopting an ether-based electrolyte instead of a carbonate-based electrolyte, the electrochemical performance of $Cu_{2-x}Se$ electrodes improved significantly. The $Cu_{2-x}Se$ electrodes exhibit outstanding cycle performance: after 1000 cycles, 160 mA h g^{-1} can be maintained with a retention of 80.3%. At current densities of 100, 200, 500, and 1000 mA g^{-1}, the capacity of a $Cu_{2-x}Se$/Li battery was 208, 202, 200, and 198 mA h g^{-1}, respectively, showing excellent rate capability. The 4-probe conductivity measurements along with electrochemical impendence spectroscopy (EIS) and cyclic voltammetry (CV) tests illustrate that the $Cu_{2-x}Se$ electrodes display high specific conductivity and impressive lithium–ion diffusion rate, which makes the $Cu_{2-x}Se$ a promising anode material for lithium–ion batteries.

Introduction

Owing to their high energy density and stable cycle performance, lithium–ion batteries have dominated the major market of portable electronic devices since the 1990s.[1] In recent years, the demand for lithium–ion batteries has increased rapidly owing to their applications in electric cars and large-scale energy-storage system.[2] However, it must be admitted that current battery technologies are not advanced enough to meet the requirements in these fields, which include high energy density, long-operation life, and reliable safety.[3] As the most commonly used anode material, the lithiation potential of graphite is below 0.2 V versus Li/Li^+. This is close to the lithium deposition potential, which may lead to the growth of lithium dendrites and cause a series of safety issues, especially at high rates.[4] Known as a zero-strain insertion material, $Li_4Ti_5O_{12}$ (LTO) shows outstanding cyclic stability. Moreover, the lithiation potential of LTO (1.5 V vs. Li/Li^+) is much higher than the lithium deposition potential, which may avoid the growth of lithium dendrites and improve the safety of the battery. These unique features make LTO an ideal anode material, thus, it has been commercialized.[5] However, the shortage of insufficient electronic conductivity (10^{-13} S cm^{-1}) and low specific capacity (175 mA h g^{-1}) impede the wide application of LTO. More efforts should be paid to find out ideal anode materials for lithium–ion batteries.

Transition metal chalcogenides such as MoS_2, FeS_2, $MoSe_2$, WSe_2, and CoSe have attracted a lot of attention.[6] Copper-based chalcogenide and its composites have been investigated because of its abundance, low cost, and high theoretical capacity.[7] Copper selenide can be found as stoichiometric and non-stoichiometric compounds, such as $CuSe_2$, CuSe, $Cu_{1.8}Se$, $Cu_{2-x}Se$, and Cu_2Se.[8] Among these compounds, $Cu_{2-x}Se$ shows unique structure and properties. The Se atoms in $Cu_{2-x}Se$ pile in face-centered cubic (*fcc*) locations (space group *Fm3m*), whereas the superionic Cu ions are disorderly distributed throughout the structure. $Cu_{2-x}Se$ shows unexpected high electrical conductivity and its conductivity increases as the deficiency of Cu increases.[9] $Cu_{2-x}Se$ could be a promising anode material, yet the application of $Cu_{2-x}Se$ as anode material for lithium–ion batteries has been rarely reported. Chen et al. prepared self-decorated $Cu_{2-x}Se$ nanosheets by a solvothermal method. The $Cu_{2-x}Se$ nanosheets show initial discharge capacity of 397 mA h g^{-1}, but the discharge capacity of $Cu_{2-x}Se$/Li half-cell fades fast; only about 37% of the initial capacity is preserved after 10 cycles.[10] One of the possible reasons for the capacity decay is the volume change of the electrode material during charge/discharge, which is a common problem of metal chalcogenides. Preparing materials with specified morphology is an effective strategy to solve this problem. One-dimensional structures (rod, wire, or tube-like structure) can preferably accommodate the volume change during charge/discharge. On the other hand, one-dimensional structures can provide enough space for diffusion of electrolyte, resulting in reduced internal resistance and improved rate performance.[7a,11] The other possible reason for the capacity fading is the side reactions between the electrolyte and the active material. Insight into the electrochemical reactions can help revealing the reaction mechanism and promoting electrochemical performance pertinently.

[a] H. Li, J. Jiang, F. Wang, J. Huang, Y. Wang, Y. Zhang, Prof. J. Zhao
State Key Laboratory of Physical Chemistry of Solid Surfaces
Collaborative Innovation Center of Chemistry for Energy Materials
State-Province Joint Engineering Laboratory of Power Source Technology for New Energy Vehicle
College of Chemistry and Chemical Engineering
Xiamen University
Xiamen, Fujian (P. R. China)
E-mail: jbzhao@xmu.edu.cn

Supporting Information for this article can be found under: https://doi.org/10.1002/cssc.201700317.

Herein, rod-like $Cu_{2-x}Se$ was prepared by a facile water evaporation process reported by Xu et al.[12] $Cu_{2-x}Se$ rods show diameters of 300–800 nm and lengths up to tens of micrometers. By substituting the carbonate-based electrolyte for an ether-based one, the electrochemical performance of the $Cu_{2-x}Se$/Li battery improves significantly. We suppose that the failure of the carbonate-based electrolyte is related with the possible reactions between Se^{2-} or Se_x^{2-} ($2 \le x \le 8$) and the carbonate solvent, which is supported by theoretical calculations. $Cu_{2-x}Se$ electrodes exhibit outstanding cycle performance: after 1000 cycles, 160 mA h g^{-1} is maintained with a retention of 80.3%. At current densities of 100, 200, 500, and 1000 mA g^{-1}, the capacity of the $Cu_{2-x}Se$/Li battery is 208, 202, 200, and 198 mA h g^{-1}, respectively, showing excellent rate capability. Electrochemical impedance spectroscopy (EIS) and cyclic voltammetry (CV) tests are performed to investigate the kinetics of $Cu_{2-x}Se$ electrodes. Furthermore, the electrochemical reactions of $Cu_{2-x}Se$ electrodes are explored by ex situ XRD.

Results and Discussion

Synthesis of rod-like $Cu_{2-x}Se$

The formation of $Cu_{2-x}Se$ rods is based on the following reactions. When Se powder and NaOH aqueous solution were mixed in a beaker and heated to about 80 °C, the Se powder reacts with NaOH into Na_2SeO_3 and Na_2Se:

$$3\,Se + 6\,NaOH \rightarrow Na_2SeO_3 + 2\,Na_2Se + 3\,H_2O \quad (1)$$

When a $Cu(NO_3)_2$ solution was added into the above solution, a CuSe deposit was formed immediately:

$$Cu^{2+} + Se^{2-} \rightarrow CuSe\downarrow \quad (2)$$

After the beaker was kept in a fan-forced oven at 140 °C, CuSe would transform into $Cu_{2-x}Se$ gradually:

$$(2-x)\,CuSe \rightarrow Cu_{2-x}Se + (1-x)\,Se \quad (3)$$

The transformation from CuSe to $Cu_{2-x}Se$ was driven from the smaller K_{sp} value of Cu_2Se (1.58×10^{-61}, whereas the K_{sp} value of CuSe is 7.94×10^{-49}) as well as the redox reaction between CuSe and the Se^{2-} anion. $Cu_{2-x}Se$ grew along the (110) direction, rod-like $Cu_{2-x}Se$ was formed eventually.[12,13]

Phase and morphology characterization

The as-prepared product was characterized by XRD and Raman spectroscopy. The XRD pattern is shown in Figure 1a; the scanning rate was 2° min^{-1} (2θ). There are several observed diffraction lines at 26.7, 44.6, and 52.9°, which match well with the (111), (220), and (311) planes of cubic $Cu_{2-x}Se$ (JCPDS No. 06-0680). No apparent impure diffraction line can be observed from the XRD pattern. Figure 1b displays the Raman spectrum of the as-prepared product. The strong and sharp band at 257 cm^{-1} is supposed to be owed to the Se–Se stretch vibration, whereas the band at 512 cm^{-1} probably corresponds to the first overtone of the strong band.[14]

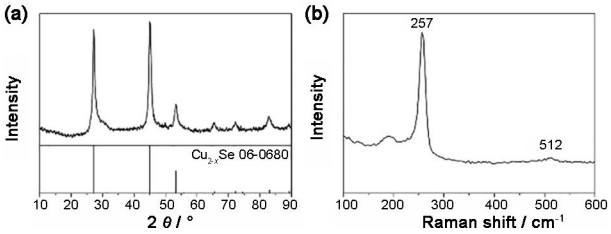

Figure 1. a) XRD pattern, b) Raman spectrum of as-prepared $Cu_{2-x}Se$.

To obtain the morphology information of synthetic $Cu_{2-x}Se$, field-emission scanning electron microscopy (FESEM) and transmission electron microscopy (TEM) tests were done. Figure 2a shows the low-magnification SEM image of $Cu_{2-x}Se$ rods, the diameter of $Cu_{2-x}Se$ rods is about 300–800 nm, whereas the length can extend up to tens of micrometers.

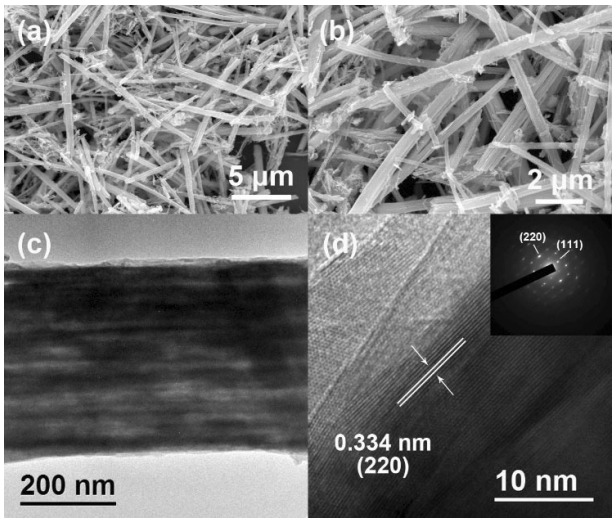

Figure 2. a, b) SEM images, c) TEM image, d) HR-TEM image and SAED pattern (inset) of $Cu_{2-x}Se$ rods.

Figure 2b reveals that the $Cu_{2-x}Se$ rods are bundled together by many thin nanowires, which can also be supported by the TEM images in Figure 2c. Figure 2d displays the high-resolution (HR)-TEM image of $Cu_{2-x}Se$ rods. The $Cu_{2-x}Se$ sample displays a highly crystalline structure. A lattice fringe spacing of 0.322 nm matches well with the (111) plane of cubic $Cu_{2-x}Se$. The selected-area electron diffraction (SAED) pattern is shown in Figure 2d (inset). The SAED pattern indicates single crystalline structure of $Cu_{2-x}Se$ rods, and the diffraction spots can be indexed to the (111) and (220) planes of cubic $Cu_{2-x}Se$.

Energy-dispersive spectroscopy (EDS) of $Cu_{2-x}Se$ rods was used to investigate the elemental composition. Figure 3a exhibits the SEM image of $Cu_{2-x}Se$ and the elemental mappings of Cu and Se are shown in Figure 3b and c, respectively. The distribution of Cu and Se elements is mainly concentrated on the rods, and the distribution of Cu and Se elements are

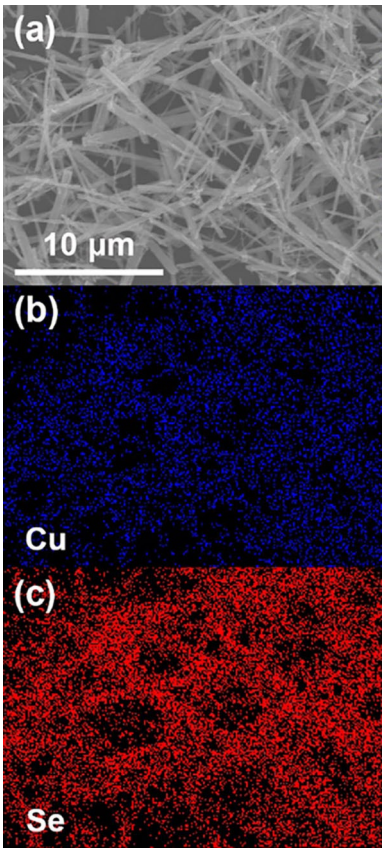

Figure 3. a) SEM image of $Cu_{2-x}Se$ rods, b) EDS mapping of Cu, c) EDS mapping of Se.

Table 1. Normalized content of Cu and Se elements, from sample shown in Figure 3.

Element	Weight [%]	Atomic [%]
Cu	60.05	64.48
Se	39.95	35.12

consistent with each other. Table 1 shows the normalized content of Cu and Se. The atomic ratio of Cu/Se is about 1.85, so the *x* value determined by EDS test is about 0.15.

The chemical state of the $Cu_{2-x}Se$ powder was characterized by X-ray photoelectron spectroscopy (XPS). The XPS survey spectrum (Figure 4a) confirms the presence of elements Cu, Se, C, and O, in whicht C and O are owed to the surface contamination that is almost unavoidable.[15] In the Cu 2p spectrum (Figure 4b), the raw data can be fitted well with peaks of $Cu\,2p_{1/2}$ (952.0 eV) and $Cu\,2p_{3/2}$ (932.2 eV). A weak satellite peak can be observed between these peaks, which means the main valence state of Cu is Cu^{+}.[16] As shown in Figure 4c, the Se 3d peak-fitting result shows $Se\,3d_{3/2}$ peak (54.5 eV) and $Se\,3d_{5/2}$ peak (53.6 eV), which matches with the spectrum of Se^{2-}.

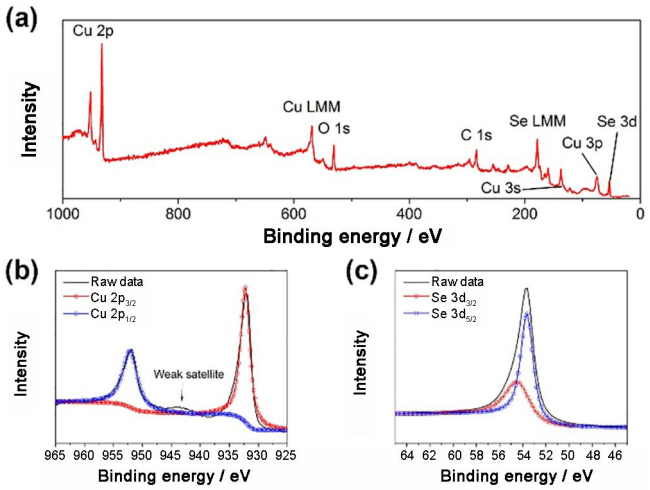

Figure 4. a) XPS survey spectrum of $Cu_{2-x}Se$ powder, detailed XPS spectra of b) Cu 2p and c) Se 3d.

Optimization of electrolyte

Chen et al. tried to apply $Cu_{2-x}Se$ nanosheets in lithium–ion batteries, but the capacity of $Cu_{2-x}Se$/Li battery declines fast. After 10 cycles, only about 37% of the initial discharge capacity can be kept and the rate performance is also unsatisfying.[10] We have noticed that they used carbonate-based EC/DEC-$LiPF_6$ (EC: ethyl carbonate, DEC: diethyl carbonate) as the electrolyte and set the discharge cut-off voltage to 0.01 V. As chalcogenides, copper sulfides usually suffer from the same problem owing to the side reactions between Li_2S or Li_2S_x ($2 \leq x \leq 8$) and carbonate solvents.[17] The effective solution is replacing the carbonate-based electrolyte with an ether-based one and raising the discharge cut-off voltage to reduce side reactions between the active materials and electrolyte.[11b,18] The same strategy may also work in the case of copper selenides. We tried both carbonate-based electrolyte EC/DEC-$LiPF_6$ and ether-based electrolyte DOL/DME-LiTFSI (DOL: 1,3-dioxolane, DME: 1,2-dimethoxyethane) as the electrolyte in $Cu_{2-x}Se$/Li half cells. The capacity–voltage plots of a $Cu_{2-x}Se$/Li battery with the EC/DEC-$LiPF_6$ are shown in Figure 5a. It can be observed that although the cell shows a clear discharge plateau in the initial discharge procedure, the capacity fades quickly. After 20 cycles, only about 29% of the initial capacity is preserved and the polarization of the battery enlarges conspicuously. After 50 cycles, the battery can be regarded as inactive. Figure 5b shows the charge/discharge curves of the $Cu_{2-x}Se$/Li battery with the DOL/DME-LiTFSI electrolyte. The battery shows an initial discharge capacity of 330 $mA\,h\,g^{-1}$, after 50 cycles, the capacity stands at 220 $mA\,h\,g^{-1}$ and the polarization of the battery reduces. Figure 5c shows the distinct comparison of batteries with different kinds of electrolytes. After 100 cycles, the capacity of the battery with the ether-based electrolyte remains at 230 $mA\,h\,g^{-1}$, whereas the capacity of the battery with the carbonate-based electrolyte is lower than 10 $mA\,h\,g^{-1}$. It is clear that the battery with the ether-based electrolyte shows much better cyclic stability than that with carbonate-based electrolyte. We also investigated the influence

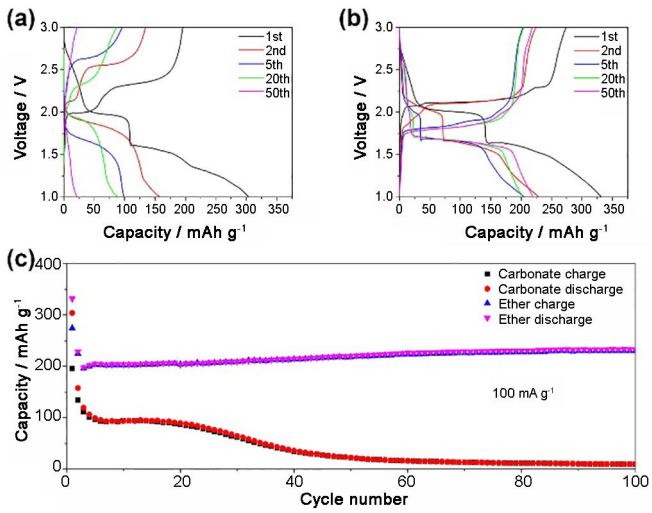

Figure 5. Charge/discharge curves of $Cu_{2-x}Se$/Li batteries with a) carbonate-based electrolyte and b) ether-based electrolyte, c) distinct comparison of $Cu_{2-x}Se$/Li batteries with different kinds of electrolytes.

of different voltage ranges. The voltage range of 1.0–3.0 V is the optimal voltage range (Figure S2 in the Supporting Information).

Electrochemical reaction mechanism

We suppose that the electrochemical reactions in the $Cu_{2-x}Se$/Li batteries are also conversion reactions like copper sulfides. Ex situ XRD (Figure 6) was performed to investigate the possible electrochemical reactions.[19] The initial charge/discharge curve is shown in the right part of Figure 6, in which point A represents the fresh battery before discharge, point B is the battery discharged to 1.8 V, point C represents the battery discharged to 1.5 V, point D is the fully discharged battery (discharged to 1.0 V), point E is the battery charged to 2.0 V, and point F represents the fully charged battery (charged to 3.0 V). The XRD samples were prepared by taking the $Cu_{2-x}Se$/Li batteries apart and removing the current collectors. XRD patterns of the electrode materials at different charge/discharge states are shown in the left part of Figure 6. After discharged to 1.8 V, the XRD pattern basically remained unchanged, yet the diffraction lines slightly shift to a lower degree, which may indicate

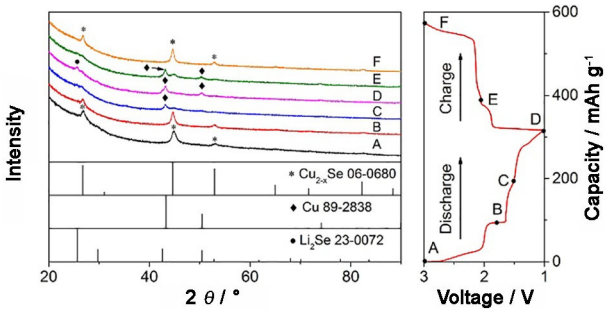

Figure 6. Ex situ XRD of $Cu_{2-x}Se$ electrodes at different states during the first discharge/charge process.

that lithium ions insert into $Cu_{2-x}Se$ to form $Li_yCu_{2-x}Se$ (the assumed molecular structure and theoretical calculation results are shown in Figures S3, S4, and S5). Patterns C and D show that both the diffraction lines of metallic Cu and the diffraction lines of Li_2Se are recognized from pattern D, which demonstrates that $Li_yCu_{2-x}Se$ is converted into Li_2Se and metallic Cu. When the battery was charged to 2.0 V, the diffraction lines attributed to metallic Cu and $Cu_{2-x}Se$ could be identified (pattern E). After charging to 3.0 V, only the XRD pattern of $Cu_{2-x}Se$ could be observed (pattern F). We assume that the charge process is the conversion from Li_2Se and Cu to $Cu_{2-x}Se$ (or $Li_yCu_{2-x}Se$, because lithium atoms are difficult to deintercalate from it). The possible electrochemical reactions can be expressed as follows:

Discharge:

$$Cu_{2-x}Se + y\,Li^+ + y\,e^- \rightarrow Li_yCu_{2-x}Se \quad (4)$$

$$Li_yCu_{2-x}Se + (2-y)\,Li^+ + (2-y)\,e^- \rightarrow Li_2Se + (2-x)\,Cu \quad (5)$$

Charge:

$$Li_2Se + (2-x)\,Cu - 2\,e^- \rightarrow Cu_{2-x}Se + 2\,Li^+ \quad (6)$$

The ex situ XRD patterns of $Cu_{2-x}Se$/Li batteries after 50 cycles were also tested (Figure S1). Diffraction lines attributed to Li_2Se and metallic Cu also can be detected after discharge to 1.0 V. It can be concluded that Se^{2-} is formed after discharge, Se_x^{2-} can be easily generated subsequently. The formation of Li_2Se and Li_2Se_x may be the key factor of the failure of carbonate-based electrolyte, so theoretical calculation was done to investigate the possible reactions between Li_2Se/Li_2Se_x and different kinds of carbonate solvents.

The bond order and bond length of Se_8 are calculated. The Se(2)–Se(3) and Se(6)–Se(7) bonds show the longest bond length and lowest bond order among these bonds (Figure 7), which indicates that they are the most unstable bonds and they are most likely to break during electrochemical reactions.[17] Thus, the major forma of Se_x^{2-} should be Se_2^{2-} and Se_4^{2-}. Possible reactions between Se_2^{2-}/Se_4^{2-} and different kinds of electrolyte solvents are investigated (Scheme 1).[20] Based on the theoretical calculation results, the Se_2^{2-} would react with the EC and the DEC spontaneously and the Se_4^{2-} would react with the EC spontaneously whereas Se_2^{2-}/Se_4^{2-} would not react with DOL or DME, which corresponds with the bad performance of $Cu_{2-x}Se$/Li batteries with carbonate-based electrolyte.

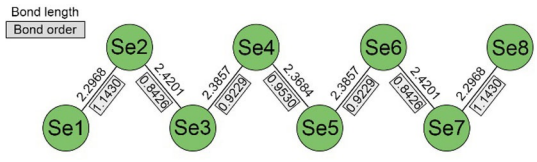

Figure 7. Bond length and bond order of Se_8.

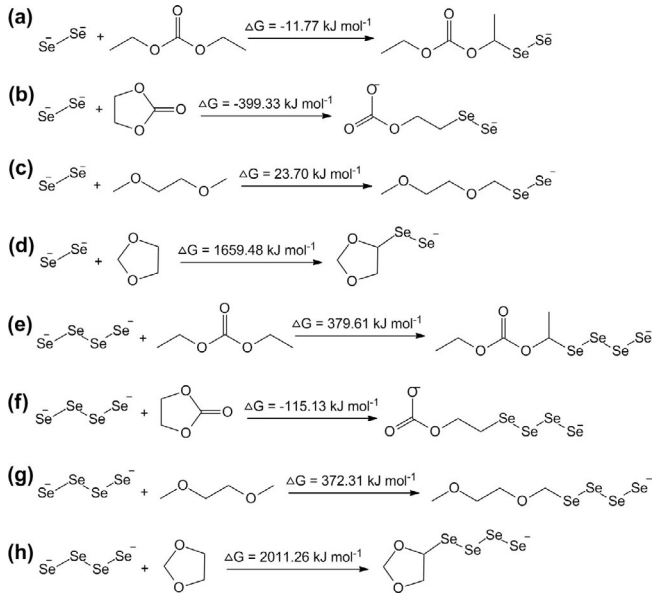

Scheme 1. Proposed reactions between Se_2^{2-}/Se_4^{2-} and different kinds of electrolyte solvents.

Electrochemical performance

The electrochemical tests were performed using ether-based electrolyte. Figure 8a shows the cyclic voltammograms of $Cu_{2-x}Se$/Li battery. During the initial cathodic scan, a reduction peak appeared around 1.9 V, which corresponds with the intercalation of Li^+ into the crystal structure of $Cu_{2-x}Se$ to form $Li_yCu_{2-x}Se$. Two peaks can be observed around 1.5 and 1.3 V; the peak at 1.3 V vanished gradually, which indicates that it may correspond with side reactions or some surface reactions.[21] The peak at 1.5 V matches with the conversion from $Li_yCu_{2-x}Se$ to Li_2Se and metallic Cu. The area of the peak around 1.9 V decreases gradually, which may be owed to the difficult extraction of lithium atoms from $Li_yCu_{2-x}Se$, therefore the insertion of Li^+ decreases. During the initial anodic scan, two distinct oxidation peaks can be observed around 1.9 and 2.2 V. These peaks correspond with the conversion from Li_2Se and Cu to cubic $Cu_{2-x}Se$. The plateau around 2.2 V vanishes after several scans, this temporary plateau may correspond with the activation of Li_2Se (like the activation of Li_2S).[7d,22] The CV test results are consistent with the charge/discharge curves in Figure 5b and the ex situ XRD results in Figure 6. The detailed electrochemical reactions can be investigated in future work by using other methods. In the subsequent scans, the reduction peaks shift to higher potentials and the oxidation peaks shift to lower potentials, which indicates the reduced polarization of $Cu_{2-x}Se$/Li battery.

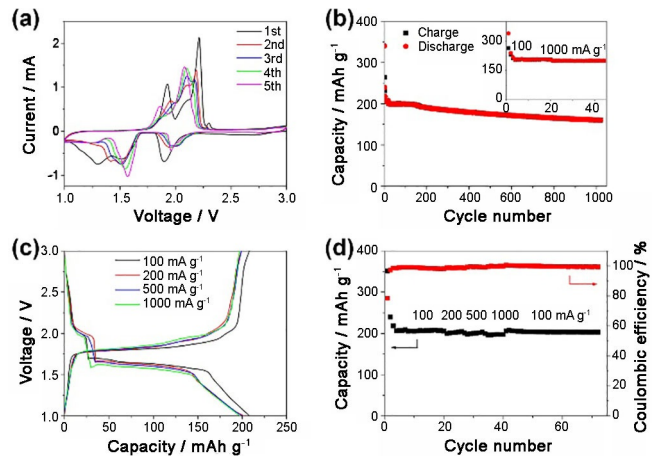

Figure 8. a) CV curves, b) cycle performance, c) capacity–voltage curves with different current densities, d) rate performance of $Cu_{2-x}Se$/Li batteries.

The long cycle performance of the $Cu_{2-x}Se$/Li battery is shown in Figure 8b. The battery was cycled at lower current density (100 mA g^{-1}) for 20 cycles first (inset), then it was cycled at high current density (1000 mA g^{-1}) for 1000 cycles. After 1000 cycles, the capacity of 160 mA h g^{-1} was kept with a retention of 80.3%. The rate performance of $Cu_{2-x}Se$/Li battery was measured at different current densities. The charge/discharge curves of the battery at different current densities are shown in Figure 8c. As the current density gets higher, the discharge plateau goes to a lower potential and the charge plateau goes slightly to a higher potential, indicating enlarged polarization of the $Cu_{2-x}Se$/Li battery at higher current density. The battery shows excellent rate performance. At current densities of 100, 200, 500, and 1000 mA g^{-1} the capacity of $Cu_{2-x}Se$/Li battery was 208, 202, 200, and 198 mA h g^{-1}, respectively. After decreasing the current density back to 100 mA g^{-1} the capacity could go back to 205 mA h g^{-1} (Figure 8d). The conductivity of $Cu_{2-x}Se$ was measured by a 4-probe conductivity measurement. The resistivity was measured to be 2.94 mΩ cm, indicating a conductivity was 340 S cm^{-1}. We believe that the impressive electronic conductivity makes a major contribution to the outstanding rate performance of $Cu_{2-x}Se$ electrodes.

EIS tests were done to investigate the kinetics of the $Cu_{2-x}Se$ electrode. The Nyquist plots of $Cu_{2-x}Se$/Li battery before and after 20 cycles are shown in Figure 9a, b. The semicircle at high frequency corresponds to the charge-transfer resistance (R_{ct}) of the $Cu_{2-x}Se$ electrode, whereas the slop at low frequency is related to the Warburg impedance of long-range Li–ion diffusion.[23] The R_{ct} decreases from 80.3 to 40.6 Ω after 20 cycles, which indicates that the surface of $Cu_{2-x}Se$ electrode gets activated and the infiltration of the electrolyte becomes batter after cycling.

CVs with different scan rates were tested using the same battery to get further insights. As the scan rate increases, the reduction peaks shift slightly to lower potentials whereas the oxidation peaks shift to higher potentials, indicating enlarged polarization of the $Cu_{2-x}Se$/Li battery (Figure 9c). According to the Randles–Sevcik equation [Eq. (7)], the peak current (i_p) is in linear relationship with the square root of the scan rate ($\nu^{1/2}$) (Figure 9d):[24]

$$i_p = 0.4463nFAC\left(\frac{nF\nu D}{RT}\right)^{1/2} \quad (7)$$

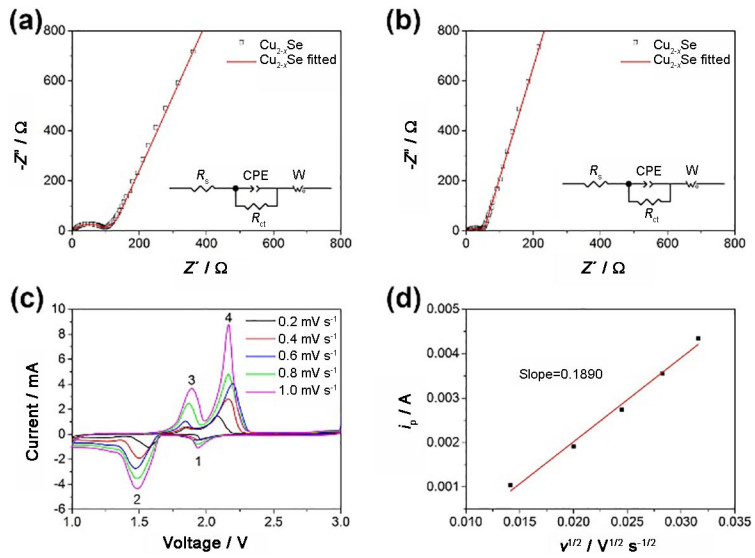

Figure 9. Nyquist plots of $Cu_{2-x}Se$/Li battery a) before and b) after 20 cycles, c) CV curves of $Cu_{2-x}Se$/Li battery with different scan rates, (d) fitted line of i_p and $v^{1/2}$.

where n is the number of electrons transferred in the redox reaction (usually equals 1), F is Faraday constant (96485 C mol^{-1}), A is the surface area of working electrode (1.14 cm^2), C stands for Li^+ concentration in the electrode (0.036 mol cm^{-3}), ν is the scan rate, R is the gas constant (8.314 J K^{-1} mol^{-1}), and T is the temperature in K. The apparent diffusion coefficient D_{CV} can be calculated with the slope of i_p–$\nu^{1/2}$ plot. The diffusion coefficient was calculated to be 2.98×10^{-10} cm^2 s^{-1} from reduction peak 2. The $Cu_{2-x}Se$ electrode shows a similar apparent diffusion coefficient to the one of the graphite electrode, exhibiting impressive diffusion rate.

Conclusions

Single crystalline $Cu_{2-x}Se$ rods were successfully synthesized by water a evaporation method. As-prepared $Cu_{2-x}Se$ rods showed a diameter of 300–800 nm and length up to tens of micrometers. By adopting an ether-based electrolyte rather than a carbonate-based one, the electrochemical performance of $Cu_{2-x}Se$ electrodes improved significantly. Li_2Se is generated through conversion reactions taken place in the $Cu_{2-x}Se$ electrodes, which can be proved by ex situ XRD tests. We suggest that the chemical reactions between Li_2Se/Li_2Se_x and the carbonate solvent may cause the failure of the carbonate-based electrolyte, which is supported by our theoretical calculations. The $Cu_{2-x}Se$ electrodes exhibit outstanding cycle performance, after 1000 cycles, 160 mAh g^{-1} was maintained with a retention of 80.3%. At current densities of 100, 200, 500, and 1000 mA g^{-1}, the capacity of $Cu_{2-x}Se$/Li battery was 208, 202, 200, and 198 mA h g^{-1}, respectively, showing excellent rate performance. The 4-probe conductivity measurements along with electrochemical impedance spectroscopy (EIS) and cyclic voltammetry (CV) tests were done to investigate the kinetics of $Cu_{2-x}Se$ electrodes, indicating the outstanding conductivity of $Cu_{2-x}Se$ electrodes (340 S cm^{-1}) and impressive lithium–ion diffusion coefficient (2.98×10^{-10} cm^2 s^{-1}). The excellent conductivity and diffusion coefficient led to the exceptional electrochemical performance of $Cu_{2-x}Se$ electrodes.

Experimental Section

Raw materials and synthesis

$Cu(NO_3)_2{\cdot}H_2O$ and NaOH (analytical reagents) were purchased from Shanghai Chemical Co., Ltd. Selenium powder (≥99.99%, metals basis) was purchased from Shanghai Aladdin Bio-Chem Technology Co., Ltd. Acetylene black (battery grade), polypropylene fluoride (PVDF, battery grade) and *N*-methylpyrrolidene (NMP, battery grade) were purchased from Guangzhou Songbai Chemical Industrial Co., Ltd. Ethylene carbonate (EC, battery grade), diethyl carbonate (DEC, battery grade), lithium hexafluoro phosphate ($LiPF_6$, battery grade), 1,2-dimethoxyethane (DME, battery grade), 1,3-dioxolane (DOL, battery grade), and lithium bis(trifluoromethanesulphonyl)imide (LiTFSI, battery grade) were bought from Zhangjiagang Guotai-Huarong New Chemical Materials Co., Ltd. All chemicals were used without any purification.

In a typical synthesis process, NaOH (5.0 g) and Se (0.15 g) were added into a 100 mL beaker, then distilled water (20 mL) was added, the beaker was heated with magnetic stirring. $Cu(NO_3)_2$ aqueous solution (1.5 mL, 0.5 mol L^{-1}) was added into the beaker after Se and NaOH formed into deep red solution. The beaker was then placed in a 140 °C fan-forced oven for 5 h. A solid product was formed on the beaker bottom as water was gradually evaporated. The product was washed by hot water and anhydrous ethanol for several times afterwards. A black powder was obtained after dried in vacuum oven at 60 °C overnight.

Material characterization

XRD patterns were recorded with Rigaku Ultima IV diffractometer (Rigaku Corporation, Japan) with CuK_α radiation source operated at 40 kV and 30 mA. The Raman spectrum was collected using a Renishaw spectrophotometer with a laser wavelength of 532 nm (Renishaw plc., UK). FESEM and EDS tests were operated by Hitachi S-4800 (Hitachi Corporation, Japan) SEM. TEM and SAED pattern were obtained from a JEM-2100 (JEOL, Japan) at the accelerating voltage of 200 kV, whereas HR-TEM and EDS linear sweep tests were obtained from a Tecnai F30 (FEI, US) at the accelerating voltage of 300 kV. XPS was tested with a PHI Quantum 2000 scanning ESCA microprobe with AlK_α radiation (1486.6 eV) (Physical Electronics, Inc. US). The conductivity was measured by 4-probe conductivity measurements on ST-2722 semiconductor resistivity of the powder tester (Suzhou Jingge Electronic Co., Ltd., P. R. China).

Electrochemical tests

The electrochemical characteristics were tested by assembling CR2016-type coin cells. Active materials, conductive acetylene black, and PVDF binder were mixed in a weight ratio of 8:1:1 in NMP to form a slurry. The slurry was coated on a copper foil and dried at 60 °C in a vacuum oven to remove the extra NMP solvent. The loading mass of active material on the electrodes was around 1.75–2.10 mg cm^{-2}. The electrode sheet was punched into round

discs. $LiPF_6$ (1 mol L^{-1}) was dissolved in the mixture solvent of EC and DEC (1:1, *v/v*) to form the carbonate-based electrolyte. Ether-based electrolyte was prepared by dissolving LiTFSI (1 mol L^{-1}) in the mixture solvent of DOL and DME (1:1, *v/v*). The Celgard 2400 (Celgard, LLC, US) was used as separator. Lithium half cells were fabricated using the prepared electrodes as positive electrodes and lithium metal as negative electrodes in an argon-filled glove box (Mbraun, Germany). The CVs were tested on a CHI 1030C multipotentiostat (Shanghai Chenhua Electrochemical Instruments, P. R. China). The galvanostatic charge/discharge tests were done on the Neware CT-3008W battery test system (Neware Battery Testing Instruments, P. R. China). All electrochemical tests were performed in the voltage range between 1.0 and 3.0 V at room temperature (25 °C). EIS tests were performed on Solartron 1260A and 1287A impedance/gain-phase Analyzer (AMETEK, UK) in the frequency range from 0.01 Hz to 100 kHz using coin cells in which lithium metal was used as the reference and counter electrode.

Calculation procedure

All calculations reported herein were performed using the Gaussian 09 computational package. All geometries were fully optimized at the B3PW91 level of DFT. There is no imaginary frequency when frequency calculations were performed at the B3PW91. The lanL2DZ basis set was used to describe Se, and the standard 6-311G + (d, p) basis set was used for H, C, and O.

Acknowledgements

This work has been financially supported by the National Natural Science Foundation of China (Grants No. 21273185 and 21321062) and National Found for Fostering Talents of Basic Science (Grants No. J1310024). Special acknowledgement is delivered to Dr. Binbin Xu and Mr. Qiming Hong in Xiamen University for their assistance in TEM tests. We also express our appreciation to Prof. Daiwei Liao in Xiamen University for his valuable suggestions and corrections on this work.

Conflict of interest

The authors declare no conflict of interest.

Keywords: copper selenide · dft calculation · electrochemical kinetics · lithium–ion batteries · x-ray diffraction

[1] M. Armand, J. M. Tarascon, *Nature* **2008**, *451*, 652 – 657.
[2] V. Etacheri, R. Marom, R. Elazari, G. Salitra, D. Aurbach, *Energy Environ. Sci.* **2011**, *4*, 3243.
[3] a) J. B. Goodenough, K.-S. Park, *J. Am. Chem. Soc.* **2013**, *135*, 1167 – 1176; b) J. B. Goodenough, Y. Kim, *Chem. Mater.* **2010**, *22*, 587 – 603.
[4] E. Peled, C. Menachem, D. Bar-Tow, A. Melman, *J. Electrochem. Soc.* **1996**, *143*, L4 – L7.
[5] a) T. Ohzuku, A. Ueda, N. Yamamoto, *J. Electrochem. Soc.* **1995**, *142*, 1431 – 1435; b) K. Zaghib, M. Simoneau, M. Armand, M. Gauthier, *J. Power Sources* **1999**, *81 – 82*, 300 – 305; c) L. Zhao, Y.-S. Hu, H. Li, Z. Wang, L. Chen, *Adv. Mater.* **2011**, *23*, 1385 – 1388.
[6] a) X. Zuo, K. Chang, J. Zhao, Z. Xie, H. Tang, B. Li, Z. Chang, *J. Mater. Chem. A* **2016**, *4*, 51 – 58; b) Z. Hu, K. Zhang, Z. Zhu, Z. Tao, J. Chen, *J. Mater. Chem. A* **2015**, *3*, 12898 – 12904; c) Z. Zhang, Y. Fu, X. Yang, Y. Qu, Z. Zhang, *ChemNanoMat* **2015**, *1*, 409 – 414; d) H. Hu, J. Zhang, B. Guan, X. W. Lou, *Angew. Chem.* **2016**, *128*, 9666 – 9670; *Angew. Chem. Int. Ed.* **2016**, *55*, 9514 – 9518; e) Y. Shi, C. Hua, B. Li, X. Fang, C. Yao, Y. Zhang, Y.-S. Hu, Z. Wang, L. Chen, D. Zhao, G. D. Stucky, *Adv. Funct. Mater.* **2013**, *23*, 1832 – 1838; f) F. Chen, J. Wang, B. Li, C. Yao, H. Bao, Y. Shi, *Mater. Lett.* **2014**, *136*, 191 – 194.
[7] a) X. Li, X. He, C. Shi, B. Liu, Y. Zhang, S. Wu, Z. Zhu, J. Zhao, *ChemSusChem* **2014**, *7*, 3328 – 3333; b) X. Wang, Y. Wang, X. Li, B. Liu, J. Zhao, *J. Power Sources* **2015**, *281*, 185 – 191; c) C. Feng, L. Zhang, M. Yang, X. Song, H. Zhao, Z. Jia, K. Sun, G. Liu, *ACS Appl. Mater. Interfaces* **2015**, *7*, 15726 – 15734; d) H. Li, Y. Wang, J. Huang, Y. Zhang, J. Zhao, *Electrochim. Acta* **2017**, *225*, 443 – 451.
[8] a) T. Liu, Z. Jin, J. Li, J. Wang, D. Wang, J. Lai, H. Du, *CrystEngComm* **2013**, *15*, 8903; b) P. Kumar, K. Singh, O. N. Srivastava, *J. Cryst. Growth* **2010**, *312*, 2804 – 2813; c) J. L. Yue, Q. Sun, Z. W. Fu, *Chem. Commun.* **2013**, *49*, 5868 – 5870.
[9] H. Liu, X. Shi, F. Xu, L. Zhang, W. Zhang, L. Chen, Q. Li, C. Uher, T. Day, G. J. Snyder, *Nat. Mater.* **2012**, *11*, 422 – 425.
[10] D. Chen, G. Chen, R. Jin, H. Xu, *CrystEngComm* **2014**, *16*, 2810.
[11] a) Y. Li, B. Tan, Y. Wu, *Nano Lett.* **2008**, *8*, 265 – 270; b) Y. Wang, X. Li, Y. Zhang, X. He, J. Zhao, *Electrochim. Acta* **2015**, *158*, 368 – 373.
[12] J. Xu, W. Zhang, Z. Yang, S. Ding, C. Zeng, L. Chen, Q. Wang, S. Yang, *Adv. Funct. Mater.* **2009**, *19*, 1759 – 1766.
[13] W. Zhang, X. Zhang, L. Zhang, J. Wu, Z. Hui, Y. Cheng, J. Liu, Y. Xie, Y. Qian, *Inorg. Chem.* **2000**, *39*, 1838 – 1839.
[14] a) B. Minceva-Sukarova, M. Najdoski, I. Grozdanov, C. J. Chunnilall, *J. Mol. Struct.* **1997**, *410 – 411*, 267 – 270; b) E. Filippo, D. Manno, A. Serra, *J. Alloys Compd.* **2012**, *538*, 8 – 10.
[15] a) D. Li, Z. Zheng, Y. Lei, S. Ge, Y. Zhang, Y. Zhang, K. W. Wong, F. Yang, W. M. Lau, *CrystEngComm* **2010**, *12*, 1856; b) J. Yang, W. Yue, X. Bo, Z. Shuyuan, Q. Yitai, *Nanotechnology* **2004**, *15*, 283.
[16] G. Deroubaix, P. Marcus, *Surf. Interface Anal.* **1992**, *18*, 39 – 46.
[17] C. Shi, X. Li, X. He, J. Zhao, *Electrochim. Acta* **2015**, *174*, 1079 – 1087.
[18] Z. Hu, Z. Zhu, F. Cheng, K. Zhang, J. Wang, C. Chen, J. Chen, *Energy Environ. Sci.* **2015**, *8*, 1309 – 1316.
[19] A. Débart, L. Dupont, R. Patrice, J. M. Tarascon, *Solid State Sci.* **2006**, *8*, 640 – 651.
[20] R. Chen, F. Wu, L. Li, Y. Guan, X. Qiu, S. Chen, Y. Li, S. Wu, *J. Power Sources* **2007**, *172*, 395 – 403.
[21] Y. Ren, H. Wei, B. Yang, J. Wang, J. Ding, *Electrochim. Acta* **2014**, *145*, 193 – 200.
[22] Y. Yang, G. Zheng, S. Misra, J. Nelson, M. F. Toney, Y. Cui, *J. Am. Chem. Soc.* **2012**, *134*, 15387 – 15394.
[23] S. S. Zhang, K. Xu, T. R. Jow, *Electrochim. Acta* **2006**, *51*, 1636 – 1640.
[24] a) H. Lin, X. Li, X. He, J. Zhao, *Electrochim. Acta* **2015**, *173*, 242 – 251; b) Y. Yang, J. Li, X. He, J. Wang, D. Sun, J. Zhao, *J. Mater. Chem. A* **2016**, *4*, 7165 – 7168; c) K. Tang, X. Yu, J. Sun, H. Li, X. Huang, *Electrochim. Acta* **2011**, *56*, 4869 – 4875.

Manuscript received: February 20, 2017
Revised: March 29, 2017
Accepted Article published: April 6, 2017
Final Article published: April 27, 2017